Heliyon 10 (2024) e40670

Contents lists available at ScienceDirect

Heliyon

journal homepage: www.cell.com/heliyon

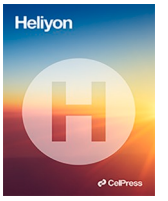

Research article

A response surface methodology study on the development of pH-sensitive wound dressings using Rhodamine B-loaded chitosan nanoparticles and sodium alginate-based films

Seyed Alireza Sheikholeslami [a], Javad Esmaeili [b,c,f], Saeedeh Zare Jalise [d], Aboulfazl Barati [e,*]

[a] Department of Chemical Engineering, Faculty of Engineering, Arak University, Arak, 38156-88349, Iran
[b] Department of Tissue Engineering, TISSUEHUB Co., Tehran, Iran
[c] Tissue Engineering Hub (TEHUB), Universal Scientific Education and Research Network (USERN), Tehran, Iran
[d] Department of Tissue Engineering and Applied Cell Sciences, School of Medicine, Qom University of Medical Sciences, Qom, Iran
[e] College of Arts and Sciences, University of Troy, Alabama, USA
[f] Department of Applied Science, UQAC University, Quebec, Canada

ARTICLE INFO

Keywords:
Nanoparticles
Smart wound dressing
Infection
Rhodamine B
Chitosan

ABSTRACT

Purpose: This study aimed to develop an innovative, intelligent wound dressing capable of signaling infections through color changes.

Design/methodology/approach: Using response surface methodology, the Rhodamine B fluorescence colorant was encapsulated within colloidal nanoparticles and integrated into a sodium alginate patch at various concentrations. The physical and chemical characteristics of the nanoparticles and the wound dressing were thoroughly analyzed via dynamic light scattering (DLS), zeta potential measurements, scanning electron microscopy (SEM), and Fourier transform infrared spectroscopy (FTIR). Additionally, the biodegradability, hydrophilicity, swelling behavior, release kinetics, porosity, mechanical properties, biocompatibility, and infection detection capability of the wound dressing were evaluated.

Findings: The results indicated that the average diameter of the synthesized colloidal nanoparticles was 300 nm before loading with Rhodamine B and increased to 400 nm after loading, with zeta potentials of 52 mV and −6 mV, respectively. The Rhodamine B-loaded wound dressing demonstrated adequate levels of swelling and hydrophilicity. Release studies revealed the gradual release of Rhodamine B at low pH. Cytotoxicity assays confirmed the high biocompatibility of the engineered wound dressing with the L929 cell line. Furthermore, bacterial exposure experiments indicated that the color change was activated in the presence of infection, making it visible under UV-A light.

Originality/value: This research presents a novel approach to wound care by developing a smart wound dressing that can detect infections via color changes. These findings underscore the potential of this innovative wound dressing to improve infection management in clinical settings through its responsive and biocompatible design.

* Corresponding author. College of Arts and Sciences, University of Troy, Alabama, USA
E-mail address: abarati@troy.edu (A. Barati).

https://doi.org/10.1016/j.heliyon.2024.e40670
Received 20 May 2024; Received in revised form 20 November 2024; Accepted 22 November 2024
Available online 23 November 2024

1. Introduction

Despite significant advances in wound dressing (WD) development, controlling wound conditions and preventing infection remain considerable challenges, accounting for a substantial portion of rapid wound healing. Due to the complex pathophysiology of wounds, bacterial-loaded wounds pose significant challenges to conventional WDs and, therefore, require the development of new and more effective wound-healing methods [1]. Wound healing typically comprises four key stages: blood clotting, inflammation, cell proliferation, and maturation [2]. Infection is a significant factor that can disrupt the healing process and delay wound closure [3]. Clinical indicators of wound infection include pain, swelling, and redness surrounding the injury [4]. Hence, early infection detection at the wound site is crucial, as it can prevent the onset of these symptomatic delays in wound healing. Neglecting the treatment of infected wounds may result in severe complications, including cellulitis, osteomyelitis, sepsis, and necrotizing fasciitis [5]. Common microorganisms present at infection sites include *Pseudomonas aeruginosa*, *Escherichia coli, Staphylococcus aureus, Staphylococcus epidermidis, and Enterobacter species* [5,6].

The advent of smart WDs aims to address the deficiency in infection surveillance during wound healing. Traditional WDs often fail to provide timely detection of infections, as the infection can go unnoticed by both patients and medical practitioners. Bacterial infections induce changes in various physical and biochemical parameters, such as temperature, pH, humidity, toxins, and enzyme release. Bacterial proliferation produces lactic acid, leading to localized acidification of the wound environment. These changes serve as detectable markers for infection surveillance and monitoring within the context of WD implementation [7]. Notably, bacterial proliferation is accompanied by the production of lactic acid, leading to localized acidification in the wound environment [8]. Consequently, within the context of WD implementation, the transformation in physical and biochemical metrics stands as discernible markers that can be harnessed for infection surveillance and monitoring [9].

The development of an innovative smart wound dressing (SWD) capable of online infection detection (OID) represents a formidable challenge within the domain of wound healing. In pursuit of this objective, scientists have harnessed the synergistic potential of biomaterials and nanotechnology to develop novel SWDs. Notably, the use of natural and chemical dyes has emerged as a promising avenue for creating color-based SWDs. In the annals of scientific advancement, a pivotal milestone was reached in 2011 when a specialized wound dressing was engineered. This pioneering SWD featured the incorporation of stabilized lipid carriers imbued with carboxyfluorescent dye, facilitating real-time monitoring of the microbiological landscape at the wound site, with a focus on the accumulation of pathogenic bacterial entities. This cutting-edge investigation entailed fabricating a patch material crafted from polypropylene, subjected to pulsed plasma treatments, and chemically modified with maleic anhydride. The modified patch material was subsequently immersed within an aqueous suspension, allowing for the attachment of dye-containing vesicles to the surface. The significance of this innovative approach lies in its capacity to transform the SWD into a dynamic sensor. Upon encountering the pernicious influence of bacterial toxins, dye-containing vesicles succumb to degradation, leading to a perceptible alteration in coloration. Specifically, discernible lightning of the green hue transpires, thereby serving as a tangible indicator of the presence of virulent bacteria within the wound environment [10]. In a comparable investigation, Thet and colleagues developed a novel WD that featured a hydrated agarose patch as its foundational substrate, with the carboxyfluorescein fluorescent dye as the pivotal detection component. The fundamental objective of this research was to encapsulate the fluorescent dye within vesicles, followed by its amalgamation with agarose and uniform dispersion throughout the hydrogel matrix. The findings from this study revealed a distinctive response mechanism characterized by the manifestation of fluorescent (light green) signals within a concise 4-h timeframe following the introduction of synthetic wound dressings into the proximity of pathogenic bacterial populations. Importantly, the sensitivity of these biopatch dressings is intricately linked to the specific species and categorization of the pathogenic bacteria encountered [11]. Subsequently, in 2020, a pH-responsive hydrogel-based SWD was innovatively crafted to deliver a sophisticated bacterial infection monitoring system. This apparatus hinged on the fluorescence resonance energy transfer (FRET) principle involving Cy3 and Cy5 fluorophores within a bacterial environment. The infection was ingeniously treated through the controlled release of antibiotics facilitated by the application of infrared light. The implementation strategy involved the encapsulation of Cy3 and Cy5 fluorophores within modified silica nanoparticles, which were thoughtfully embedded within the hydrogel dressing. At reduced pH levels, notable spatial proximity between Cy3 and Cy5 was achieved, with their separation distance reduced to a mere 10 nm, inducing the FRET phenomenon. Up-conversion nanoparticles (UCNPs) were thoughtfully incorporated into the hydrogel matrix to augment this system's capabilities, thereby facilitating the conversion of incident light spectra into ultraviolet wavelengths upon irradiation. This catalytic process led to the disintegration of the bond connecting gentamicin sulfate to the hydrogel, ultimately liberating gentamicin to combat bacterial infections with efficacy [12].

In this work, we propose an innovative SWD with the capability of OID. This SWD incorporates Rhodamine B (RB) fluorescence colorant encapsulated within colloidal nanoparticles (RCNPs) and integrated into a sodium alginate (SA) patch. By optimizing the concentration of RCNPs in the SA patch via response surface methodology, we aimed to create a responsive and biocompatible WD that signals infections through visible color changes under UV-A light.

Our research introduces a novel approach to wound care by combining biomaterials and nanotechnology to develop a color-based SWD. This SWD is designed to detect infection through pH-sensitive color changes, providing real-time feedback on wound status. This work aims to enhance infection management in clinical settings by offering a smart, biocompatible wound dressing that improves patient outcomes through timely and accurate infection detection.

2. Materials and methods

2.1. Chemicals

Chitosan (70 % deacetylated, low viscosity), sodium alginate (low viscosity), and sodium bicarbonate were procured from Sigma Aldrich. Sodium triphosphate (TPP), glycerol, calcium dichloride, acetic acid, and various other reagents were supplied by a local vendor (AlborzShimi Co., Iran). The fluorescent dye rhodamine B (RB) was also obtained from Merck.

2.2. Preparation of chitosan nanoparticles

The ionization technique was harnessed to fabricate chitosan nanoparticles (CNPs) [13]. This approach capitalizes on the electrostatic interaction between the positively charged amino groups of chitosan and the negatively charged sodium triphosphate (TPP) groups. To produce CNPs via this methodology, a chitosan solution at a concentration of 5 mg/ml in 1 % acetic acid was prepared at ambient temperature, ensuring clarity and the absence of undissolved particulate matter. The pH of the chitosan solution was subsequently adjusted to a precise level of five through the judicious addition of 1N sodium hydroxide. The calculated volume of TPP solution, also at a concentration of 5 mg/ml, was introduced dropwise into a predetermined quantity of the chitosan solution, maintaining a ratio of 3.3:1, and the mixture was agitated for 2 h. The resulting CNPs were isolated through centrifugation and subjected to three successive washing cycles with distilled water.

2.3. Preparation of RB-loaded CNPs

In the synthesis of RB-loaded chitosan nanoparticles (RCNPs), the procedure commenced with the preparation of a chitosan solution at a concentration of 5 mg/ml, with the pH meticulously adjusted to 7. Concurrently, the fluorescent dye RB was introduced at a

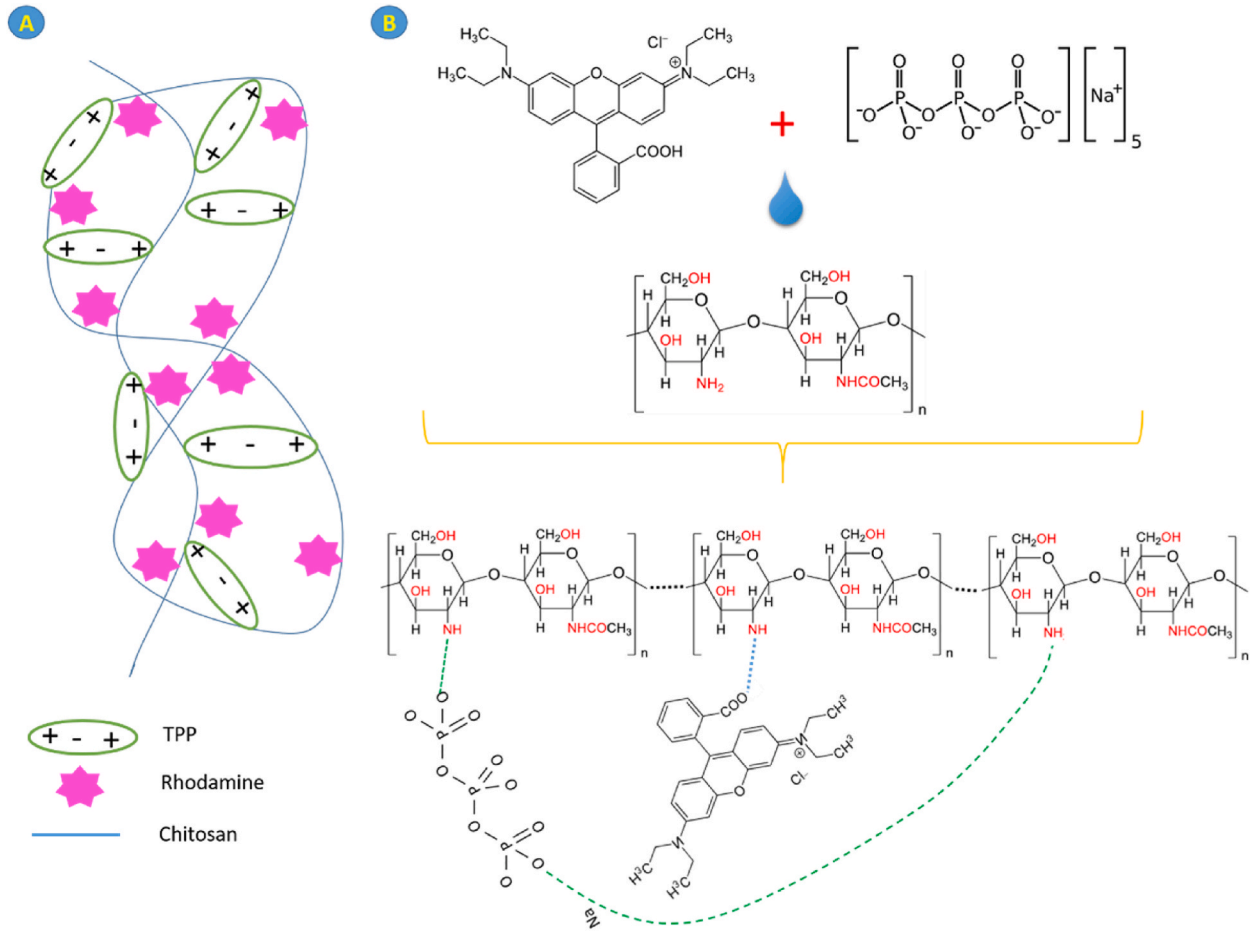

Fig. 1. Schematic of the recommended mechanism for synthesizing RCNPs. A) RCNP synthesis method, and B) The primary bonding mechanism between TPP, RB, and chitosan.

0.1:1 ratio of chitosan into a TPP solution of 5 mg/ml. The vigorous stirring of these solutions was sustained for 1 h, and the samples were maintained at room temperature. The resulting solution was subsequently introduced dropwise into the chitosan solution. The resulting nanoparticles were subjected to a triple-round washing regimen and centrifugation, with each round executed at 4000 rpm. Fig. 1A shows the RCNP synthesis method, and Fig. 1B depicts the primary bonding mechanism between TPP, RB, and chitosan.

2.4. Fabrication of CNP-loaded films

Using Design Expert software (Version 13), a set of experiments was designed, with SA films containing varying SA contents (ranging from 1 to 2 % w/v) and chitosan nanoparticles (CNPs) in the range of 1–10 % w/w SA by weight. This represented the two vital independent parameters, constituting a comprehensive experimental matrix conducted in 20 ml volumes, as summarized in Table 1. To optimize the formulation of the final RCNP-loaded film, the response surface methodology (RSM) technique was judiciously applied, explicitly employing central composite design (CCD). This statistical approach was instrumental in efficiently managing the experimental groups and identifying an ideal formulation within the scope of the primary parameters under scrutiny [14,15]. The critical responses under evaluation encompassed degradability, swelling behavior, contact angle, and mechanical strength, collectively forming the crux of the study's assessment.

As per the proportions outlined in Table 1, a predetermined quantity of SA was solubilized in 20 ml of distilled water. The stirring protocol spanned 2 h, maintaining operational conditions at 400 revolutions per minute (rpm) and a temperature of 25°C. To impart enhanced flexibility to the final film, an increment of 200 μl of glycerol was introduced [16]. The requisite RCNP was subsequently amalgamated with the SA solution. A thorough mixing process was executed, lasting 1 h and adhering to the exact parameters of 400 rpm and a temperature of 25°C. The culmination of this process involved the use of casting and solvent evaporation techniques, which produced the final RCNP films. To reinforce the structural integrity of the films, a 10 % calcium chloride solution was employed for cross-linking purposes [17]. The film samples underwent a dual-stage cleansing process involving two sequential rinses with distilled water.

2.5. Investigation of nanoparticle morphology

CNPs, RCNPs, and films were morphologically evaluated by scanning electron microscopy (SEM VEGA3). For the NPs, a small portion of the CNPs and RCNPs were sonicated separately and then placed on aluminum foil. Finally, they were coated with gold NPs. The film was dried and coated with AuNPs [18].

2.6. Fourier transform infrared spectroscopy

In material identification, a fundamental technique that assumes a prominent role is Fourier transform infrared spectroscopy (FTIR Thermo Avatar). Within this investigation, the scope of FTIR analysis was rigorously applied across the spectral range spanning 400–4000 cm^{-1}, encompassing the evaluation of CNPs, RCNPs, and the RB. This analytical approach facilitates a nuanced exploration of the molecular composition and chemical characteristics of the entities under scrutiny [19].

2.7. DLS and zeta potential

The surface charge and hydrodynamic diameter of the CNPs and RCNPs were measured via the dynamic light scattering (DLS NanoDS) method. First, the NPs were diluted twice in water and sonicated. Then, it was transferred to a particular device cell, and measurements were carried out [18].

Table 1
Experimental design parameters.

Run	Factor A: SA (%)	Factor A: Chitosan (%)
1	2	10
2	1.5	5.5
3	1	10
4	1.5	1
5	1.5	5.5
6	1.5	10
7	1	1
8	2	5.5
9	1.5	5.5
10	2	1
11	1.5	5.5
12	1.5	5.5
13	1	5.5

2.8. RB standard curve

The standard curve of RB was generated by preparing solutions with known concentrations and measuring their absorption via a UV–vis spectrophotometer. Ten standard solutions were prepared via the dilution method. The absorption of the prepared solution was measured at 554 nm.

2.9. RB release study

The release of RB from both RCNPs and the RCNP-loaded film was examined via a dialysis bag. In this context, predetermined quantities of RCNPs and RCNP-loaded films were enclosed within a dialysis bag immersed in distilled water. The experimental parameters included distinct pH levels, namely, 4, 7, and 10, and ambient conditions at 25°C. The system was gently agitated at regular intervals, specifically at 3-, 6-, 24-, 48-, and 72-h time points. At each prescribed interval, a precise volume of 5 ml from the solution was carefully withdrawn for quantitative assessment, after which it was reinstated in the solution. The liberated RB was quantified through reference to a standard curve, thereby providing comprehensive insight into the release dynamics of the compound from both RCNPs and the RCNP-loaded film [20].

2.10. Swelling

Following the drying process at a regulated temperature of 33 °C, the RCNP-loaded films were subjected to thickness measurements employing a micrometer, denoted as "h_0." The samples were subsequently immersed in distilled water, and after a 3-h incubation period, they were extracted from the aqueous environment [21]. To ascertain the extent of water absorption, any residual liquid was methodically eliminated via filter paper, and the thickness of the samples was reevaluated, denoted as "h_t". The degree of swelling of the films was calculated via Eq. (1):

$$\% \text{ Swelling} = \frac{(h_t - h_0)}{h_0} \times 100 \quad (1)$$

2.11. Biodegradability

The degradation analysis involved the periodic measurement of film weight loss over distinct time intervals. Each film, initially of known weight (denoted as W0), was sectioned into 2 × 2 cm^2 segments. These film segments were subsequentfig3ly immersed in Petri dishes containing 15 ml of distilled water and maintained at 37°C throughout the incubation period [22]. The film segments were retrieved from their respective environments at specific time points, which included days 1, 3, 7, and 14. After extraction, any residual water was eliminated, and the segments were reweighed, and their new weight (Wt) was determined. The degree of degradation was calculated by Eq. (2):

$$\% \text{ degradation} = \frac{(W_t - W_0)}{W_0} \times 100 \quad (2)$$

2.12. Mechanical properties

The tensile strength according to the ASTM D 638 standard was measured to determine the mechanical behavior of the films via SANTAM STM-20. A 50 N force at a rate of 1 mm/min was applied to the samples to the point of rupture, and a stress–strain diagram was drawn. The test was performed with three replications [23].

2.13. Contact angle

Contact angle measurement is a pivotal gauge for delineating the wettability characteristics of a solid surface about a liquid. This metric, expressed as an angle, provides insights into the surface's hydrophobic or hydrophilic nature. In our study, the determination of contact angles was executed by precisely placing water droplets onto the film surface. Subsequently, the angle between the film's surface and the contact droplet was meticulously assessed utilizing Digimizer software.

2.14. Cytotoxicity

One of the paramount attributes inherent to dermal WDs within the realm of skin tissue engineering lies in their profound capacity for engagement with cellular constituents facilitated through the application of the MTT assay [24]. In the procedural sequence, the SA film underwent initial sterilization via exposure to UV radiation, followed by subsequent immersion in sterile phosphate-buffered saline (PBS) to purge contaminants. These substrates were subsequently colonized at a density of 1 × 10^4 mouse skin fibroblast (L929) cells per well, the introduction of which was orchestrated with meticulous precision through a droplet technique executed in a 96-well culture plate. The mixture was incubated for 48 h at 37°C in a 5 % CO2 atmosphere to promote the cellular microenvironment. Following this incubation, an aliquot of 100 μl of MTT (3-(4,5-dimethylthiazol-2-yl)-2,5-diphenyltetrazolium bromide) solution,

prepared at a concentration of 5 mg/ml, was introduced into each well, subsequently resulting in a 4-h incubation interval. To ensure the seamless execution of these steps, the contents of every well underwent methodical aspiration, followed by the addition of 100 μl of dimethyl sulfoxide (DMSO). In the culmination of this intricate procedure, the quantification of light absorption, predicated upon cellular metabolic activity, was meticulously and discerningly documented, employing an ELISA reader (BioTec) that operates at a wavelength of 570 nm. The cell viability was calculated via Eq. (3):

$$\%\ \text{cell viability} = \frac{\text{mean Abs of sample}}{\text{mean Abs of control}} \times 100 \tag{3}$$

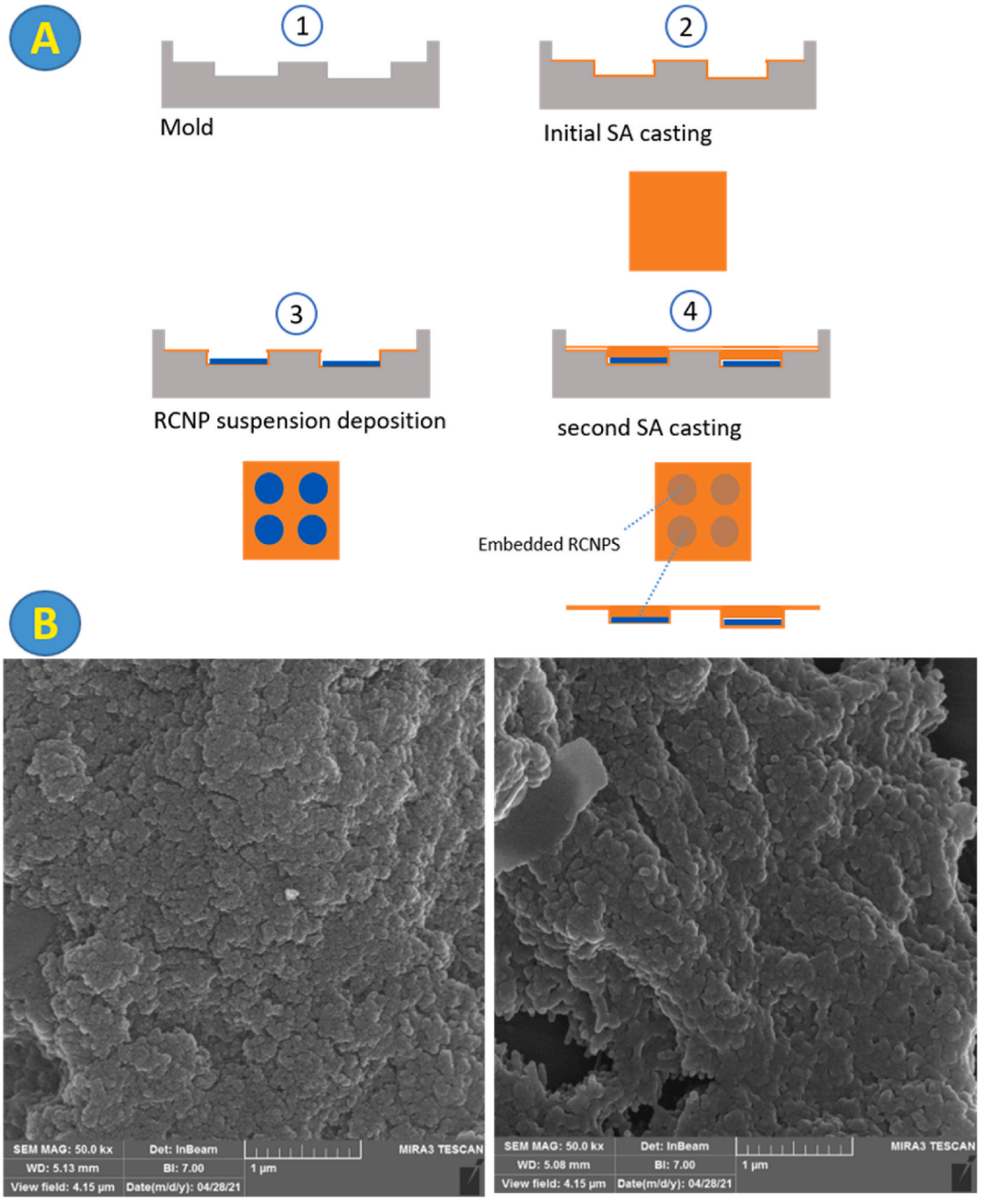

Fig. 2. A) Schematic protocol to fabricate the final RCNP-loaded patch. B) SEM analysis of CNPs (left) and RCNPs (right).

2.15. Fabrication of the final RCNP-loaded wound dressing patch

After the data were carefully evaluated and the recommended formula was analyzed via the CCD approach, one formula was used to obtain the final RCNP-loaded WD patch. To achieve this goal, as shown in Fig. 2A, a 1 × 1 cm^2 mold with four circular cavities (d = 8 mm, depth = 2 mm) was fabricated using an acrylic sheet. First, 1 ml of the SA solution was poured into the mold and left at room temperature to dry. Then, 50 λ of the RCNP suspension was emptied into each cavity and incubated at 37 $^{\circ}C$. Then, 1 ml of SA solution was poured into the mold again. The mold was then incubated at 37 $^{\circ}C$ for 24 h. The final dried RCNP-loaded patch was used for infection detection.

2.16. Detection of infection

The efficacy of the RCNP-loaded patch in combating two distinct bacterial strains, *Escherichia coli* (*E. coli*, gram-negative) and *Staphylococcus aureus* (*S. aureus*, gram-positive), within a bacterial growth medium was assessed. Isolated *E. coli and S. aureus* bacterial cultures were cultivated primarily on individual plate count agar (PCA) plates. The RCNP-loaded patch was subsequently positioned at the geometric center of each respective culture plate. These prepared plates were then subjected to an incubation period of 24 h. Using ultraviolet type A light, changes in the light in the patch were monitored visually.

2.17. Statistical analysis

We utilized Design-Expert® software version 13 and conducted a one-way analysis of variance (ANOVA) to assess differences and analyze the results. The results are presented as the means ± standard deviations, and statistical significance was set at $P < 0.05$ for all factors.

3. Results and discussion

Fig. 2B shows SEM images of NPs with a consistent spherical structure. The inclusion of RB clearly caused an increase in the size of the RCNPs but did not significantly alter their shape. According to a study by Song et al. (2024), including riboflavin (RB) in polymeric nanoparticles also increases size, which they attributed to the interaction between RB and the polymer matrix, causing expansion of the

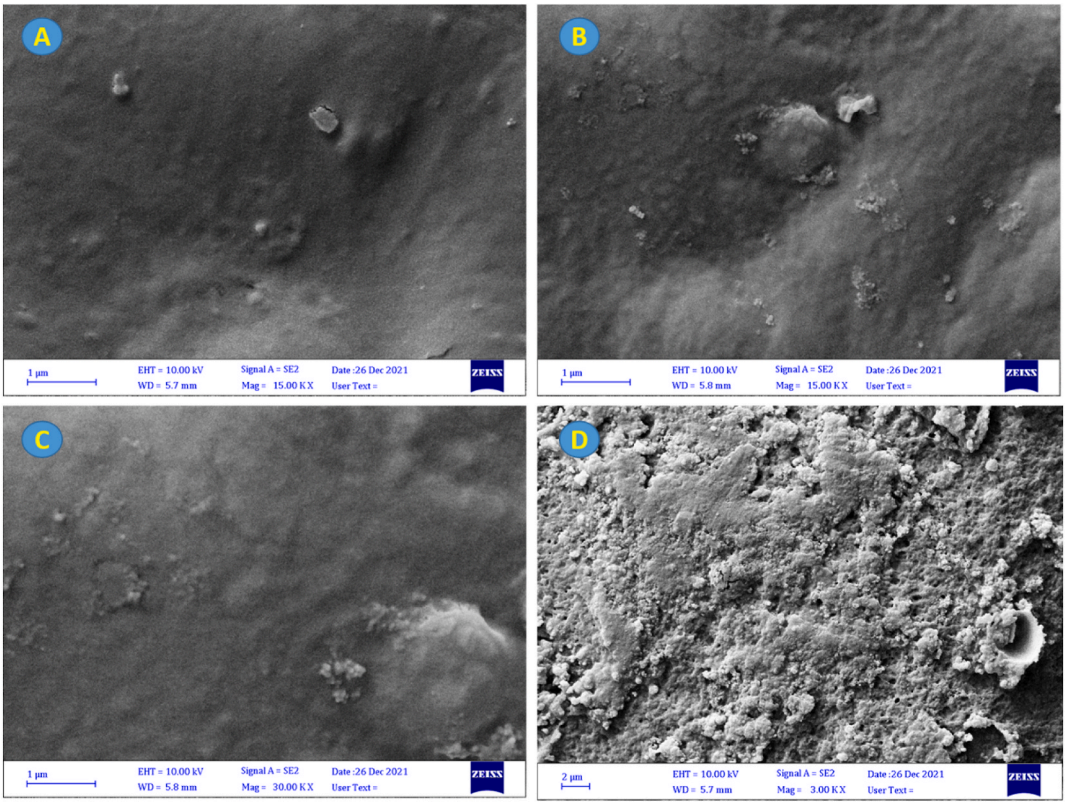

Fig. 3. Scanning electron microscopy (SEM) images of sodium alginate films with concentrations of A) 1 %, B) 1.5 %, and C) 2 %. D) SEM images of the deposited RCNPs according to Fig. 2A.

nanoparticle structure. The shape remained largely spherical, which is consistent with our observations [25]. Furthermore, Wu et al. (2015) demonstrated that adding certain compounds to nanoparticles can increase their size without changing their spherical morphology. This effect was attributed to the physical and chemical interactions between the additive molecules and the nanoparticle matrix [26]. Fig. 3A–C shows SEM images of the surfaces of SA films with varying concentrations, demonstrating their uniformity and the absence of surface defects such as cracks or pores. Crosslinking is expected to enhance the quality and consistency of these films [27]. A study by Bhagath et al. (2022) revealed that sodium alginate (SA) films, when properly crosslinked, exhibit a uniform surface free of defects such as cracks and pores. This is attributed to the efficient crosslinking process that stabilizes the film structure [28]. Research by Li et al. (2019) revealed that crosslinking improves the mechanical properties and surface uniformity of SA films, supporting the idea that crosslinking enhances film quality [29]. Furthermore, Fig. 3D shows the surface of the deposited RCNPs via the procedure outlined in Fig. 2A. These images demonstrate that the RCNPs are consistently stacked atop one another, resulting in a uniform layer. Studies on nanoparticle deposition techniques, such as those by Kumar et al. (2022), have shown that uniform layer

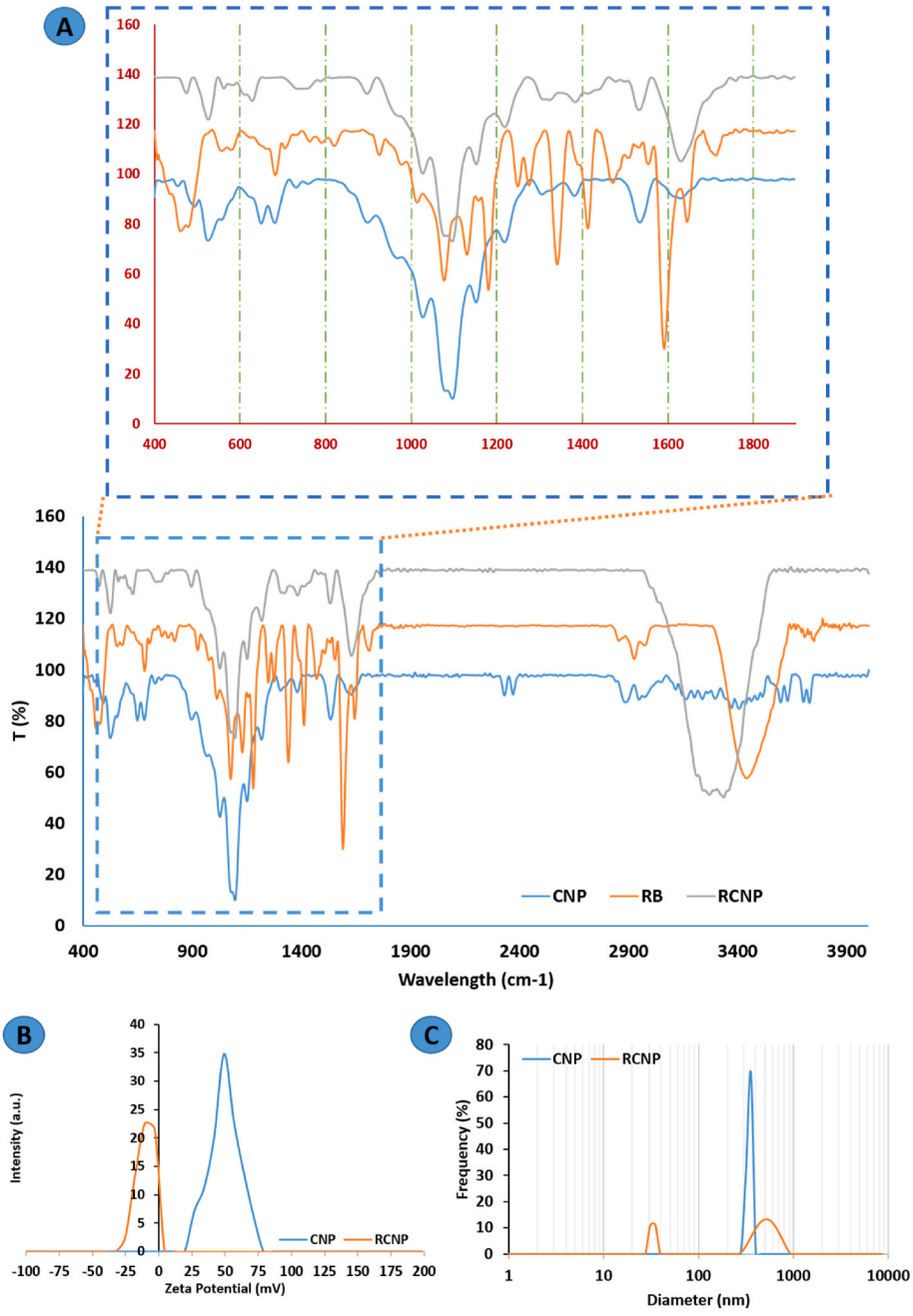

Fig. 4. A) FTIR spectra of CNPs, RBs, and RCNPs; B) zeta potential; and C) size distribution (DLS) of CNPs and RCNPs.

formation is critical for applications in coatings and films. Consistent stacking without significant aggregation indicates a controlled deposition process, similar to our findings [30]. Chen et al. (2015) demonstrated that a uniform nanoparticle layer is achievable through careful control of the deposition parameters, ensuring that the nanoparticles are evenly distributed and stacked, enhancing the functional properties of the film [31].

Fig. 4 presents the FTIR spectra of CNPs, RCNPs, and RB. The CNP spectrum confirmed the presence of free amine, hydroxyl, and ether groups [32]. In Fig. 4A, an observable peak spanning the 3300–3700 cm^{-1} range corresponds to OH tensile groups, intramolecular hydrogen bonds, and the presence of amines [33]. Peaks at 2947.32 cm^{-1}, 2884.15 cm^{-1}, 1381.36 cm^{-1}, and 1629.11 cm^{-1} represent the NH3 functional group, CH absorption band, NH flexural vibration, and CH flexural vibration of the alkyl group, revealing the interaction between the chitosan and phosphate groups, specifically TPP [34]. Additionally, the appearance of a peak at 1026.66 cm^{-1} indicates the P=O tensile vibration characteristic of phosphate groups [35]. Absorption peaks within the 680–1059 cm^{-1} range are attributed to the antisymmetric tensile vibration of C–O–C steps within the chitosan matrix [36].

According to Fig. 4A, specific peaks can be identified: the 2924.96 cm^{-1} and 1712.26 cm^{-1} peaks, along with those spanning 1506.72 cm^{-1}–1644.82 cm^{-1}, suggest the presence of CH tensile bands and C=O ester functionalities. Furthermore, these peaks indicate the existence of C=C, C=N, and C=O bonds [37]. The 1591.22 cm^{-1} peak corresponds to the C=O tensile band of amides. The peak at 1412.71 cm^{-1} is attributed to the tensile vibration of the benzene ring [38]. The peaks at 1341.19 cm^{-1}, 1249.02 cm^{-1}, and 1076.47 cm^{-1} are associated with the bending of the CH_3 bond, C–OH stretch, and C–N stretch, respectively [39]. The appearance of peaks within the 898–617 cm^{-1} range indicates aromatic vibrations [40]. The alterations and presence of oscillations in the RCNP spectrum, compared with the color spectra of rhodamine and CNPs, confirmed the presence of both substances in the nanoparticles. Notably, the increased intensity of the peak at 1644 cm^{-1} reflects the loading of RB in CNPs. In contrast, the RCSN spectrum does not exhibit the absorption of carboxyl groups at 1700 cm^{-1}, which is present in the pure RB spectrum. The newly observed peak at 1647 cm^{-1} can be attributed to the amide I group, underscoring the interaction and entanglement of RB with CSN (Fig. 1A).

As shown in Fig. 4B, the results of the zeta potential analysis revealed that the CNPs and RCNPs presented surface charges of +51.9 mV and −6.3 mV, respectively. Previous investigations have established that chitosan NPs typically possess a positive potential within 39–45 mV [41]. Studies have consistently reported a negative surface charge for chitosan nanoparticles loaded with RB [42]. The shift from a positive to a negative surface charge in RCNPs can be attributed to the presence of RB, confirming the bonding between RB and CNPs. Consequently, a greater quantity of rhodamine in CNPs results in a more negative surface charge, indicating repulsive forces among the RCNPs and their non-aggregating nature, which, in turn, contributes to the stability of the synthesized nanoparticles.

The NP size distribution analysis was conducted via DLS, and the findings are presented in Fig. 4C. The results revealed that the CNPs had an approximate diameter of 300 nm. In contrast, the RCNPs were predominantly in the 400–500 nm range. The increase in RCNP size can be attributed to two factors: i) the incorporation of RB and ii) the incomplete dispersion of RCNPs. The mean sizes obtained for the CNPs and RCNPs were 308.5 nm and 393.2 nm, respectively. Notably, encapsulating a drug can increase nanoparticle size [43].

In this investigation, by employing the CCD methodology, we examined the swelling characteristics of films and the impact of incorporating RCNPs into SA films on the swelling rate. As demonstrated in Fig. 5A, the degree of swelling is directly correlated with the SA content. This correlation is attributed to the increased hydrophilicity of SA, resulting from the presence of hydrophilic functional groups such as NH_2, OH, and COOH, which foster stronger interactions with water molecules, leading to increased water

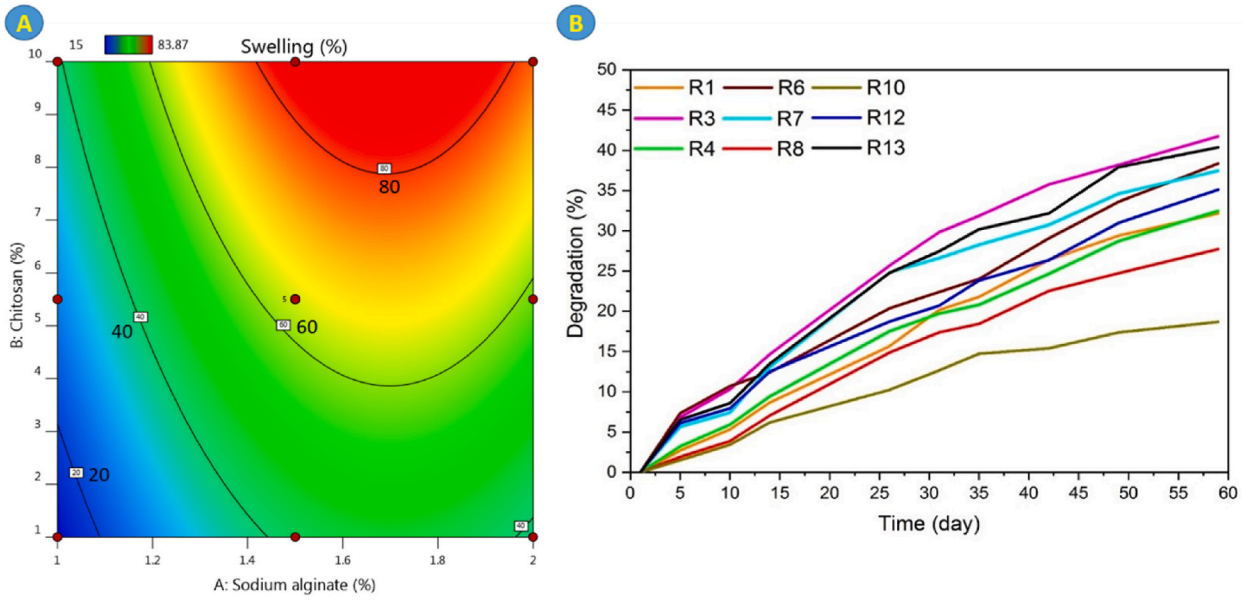

Fig. 5. A) Counterplot of the swelling of SA films. B) Results of the degradation of SA films over 60 days.

absorption [44]. Additionally, an increase in RCNP content led to increased swelling, particularly in films with higher SA contents (1.4–2%). Moreover, as the SA percentage increased, the degree of swelling increased from 20 % to 83.7 %. This behavior can be explained by the strengthening of hydrogen bonds between SA molecules as the concentration of SA in the solution increases [14].

Fig. 5B provides insights into the degradation process. It becomes evident that a higher RCNP concentration in conjunction with a low SA content accelerates degradation, whereas a lower RCNP content and a higher SA percentage yield reduced degradation rates. This observation aligns with previous discussions regarding the enhanced water uptake and swelling resulting from the presence of RCNPs, which directly influences the degradation rate [45]. The mechanism underlying this behavior involves the swelling and subsequent dissolution of RCNPs, causing the disintegration of SA bonds and, consequently, hastening degradation. The degradation of chitosan in distilled water primarily occurs through the participation of OH and NH_2 groups, which engage in hydrogen bonding interactions with water molecules [46].

Table 2 presents the results for the tensile strength, elastic modulus, and elongation at break of the SA films loaded with RCNPs. Table 2 alongside the results of the CCD analysis (Fig. 6A) reveals that the highest elongation values are found in the R1 sample. The tensile strength and elongation are directly related to the SA content. This relationship is explained by the assumption that as the SA percentage increases, the number of SA molecules per unit volume increases. This increases the number of hydrogen bonds between the molecules, resulting in enhanced cross-linking and the formation of a more compact lattice structure, consequently leading to greater mechanical strength [47]. In contrast, the addition of RCNPs introduces mobility and elasticity to the lattice structure because of the strong ionic interactions between the RCNPs. This interaction enhances elongation [48]. Notably, mechanical behavior can vary across different cases, depending on factors such as nanoparticle type, concentration, and the specific biomaterial employed.

Skin tissue is known for its capacity to expand and contract easily during movement. Sample R2 exhibited a heightened level of elasticity, primarily due to its higher SA content. As depicted in Fig. 6B, the elastic modulus, which is the ratio of stress to strain, of SA films is minimally affected by the quantity of RCNPs and is predominantly contingent on the SA content [49]. This differs from previous studies in which the nanoparticle concentration was a pivotal factor influencing the mechanical strength [50]. In this context, the film with 2 % SA and 1 % chitosan nanoparticles displayed the lowest elastic modulus.

The results obtained from the stress analysis provide insights into the load-bearing capacity of the test samples. As shown in Table 2 and Fig. 6C, R1 clearly has the highest tolerance to applied force compared with the other films. Moreover, a positive correlation exists between the percentage of SA or RCNPs and the stress-bearing capacity of the film [51].

Water contact angle measurements serve as indicators of the hydrophilic or hydrophobic nature of materials. Typically, materials with low contact angles are considered hydrophilic. In this study, the contact angle for all the films was approximately 50 $\pm$ 5°, indicating the pronounced hydrophilic characteristics of the RCNP-loaded films. A study by Jonderian et al. (2016) specifically examined RCNP-loaded films and reported water contact angles of approximately 50°, which is consistent with our results. This finding indicates that RCNPs contribute to the hydrophilic nature of the films [52]. Wang et al. (2016) analyzed RCNP-loaded films and reported contact angles in the range of 48–55°, supporting the pronounced hydrophilicity observed in our study [53].

One of the main outputs of RSM-based studies is proposing mathematical models to predict the responses (dependent parameters) under any conditions for independent parameters (SA and RCNP).

The swelling, degradation, contact angle, and mechanical behavior, as responses, were investigated and the appropriate models were proposed. Based on these results and RSM analysis, the recommended models were as below (Table 3), where "A" stands for the SA concentration and "B" stands for RCNP content.

As previously mentioned, RSM is a statistical and mathematical approach used to model and optimize processes affected by multiple variables. It allows researchers to build polynomial regression models (typically quadratic) that approximate relationships between independent parameters and the desired responses. One of the main benefits of RSM is in complex studies where the exact interactions between parameters are unknown. By fitting these regression models, RSM enables predictions of response values and helps identify optimal conditions that either maximize or minimize the response. Considering Table 3, *A, B, AB, A2,* and B^2 represent different types of effects on the response. *A* and *B* are the main effects of each independent input. They represent the direct, linear relationship between each variable and the response. The higher coefficient for each means the more impact of that parameter. *AB* is the interaction effect between *A* and *B* meaning that how the effect of *A* on one response alters depending on the level of *B*. *A2* and B^2

Table 2
Tensile test results of samples.

sample	Stress (MPa)	Elongation (%)	Module (MPa)
R1	1.16	2.95	39.26
R2*	0.97	1.68	57.80
R3	0.53	1.05	50.48
R4	0.86	1.48	58.47
R5*	0.97	1.68	57.80
R6	1.01	1.62	62.31
R7	0.61	0.62	98.38
R8	0.83	2.92	28.66
R9*	0.97	1.68	57.80
R10	0.57	2.44	23.55
R11*	0.97	1.68	57.80
R12	0.97	1.68	57.80
R13	0.81	0.98	82.65

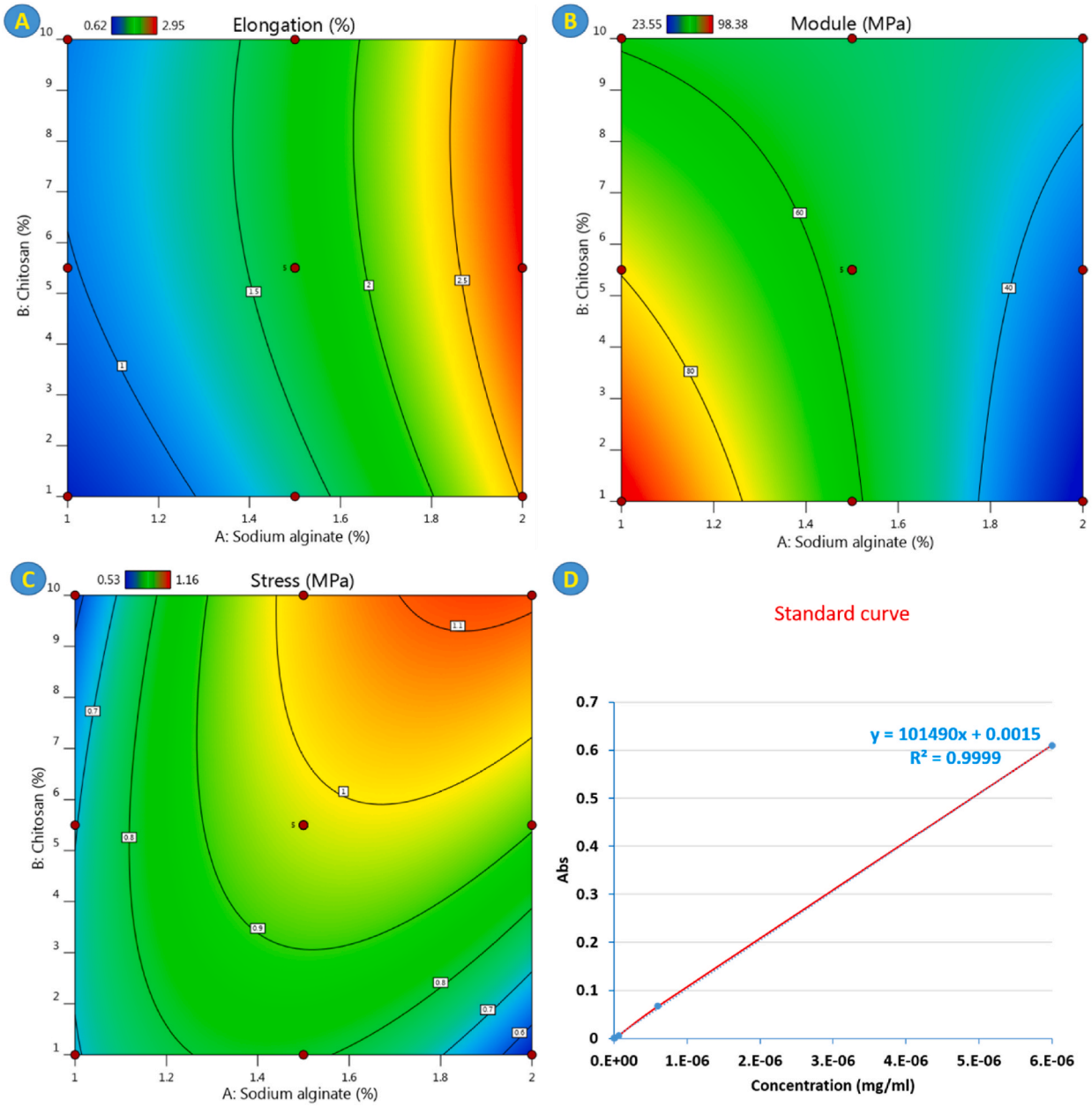

Fig. 6. Counterplots of A) elongation, B) elastic modulus, and C) stress at break. D) Standard curve for RB release.

Table 3
Proposed numerical models for the responses by RSM.

Model	P-value	R^2
$(\mathbf{Module})^{1.11} = +88.44-20.24A-8.85B + 27.66AB$	<0.0001	0.945
$(\mathbf{Elongation})^{0.85} = +1.56 + 0.7396A + 0.4036B-0.1046AB-0.1329A^2-0.1593B^2$	<0.0001	0.992
$(\mathbf{Stress})^{1.68} = +0.9570 + 0.1536A + 0.1739B + 0.2465AB-0.0257A^2-0.0777B^2$	<0.0008	0.926
$(\mathbf{Swelling})^{0.33} = +3.94 + 0.4391A + 0.4465B + 0.0410AB-0.0263A^2-0.0559B^2$	<0.0001	0.994
$\mathbf{Degradation} = +35.37-6.84A + 3.91B + 2.34AB-1.96A^2-0.5850B^2$	<0.0001	0.985

are quadratic (or curvature) effects for each independent value. They show the linear or nonlinear relationships, showing the linear or non-linear changes in the response as A or B alters [54].

Keeping this information in mind, as you can see in Table 3, R^2 for all models was close to one confirming the reliability of the

models. Besides, the P-value for all models was extremely less than 0.05 confirming the significance of the model. Focusing on *A* (SA content) and *B* (RCNP), it can be concluded that each one has a direct impact on the response. Regarding *AB*, it can be seen that both *A* and *B* affect each other about the mechanical responses. Regarding swelling it can be stated that they do not affect each other significantly. Results show that changes in *A* affect the impact of *B* on degradation and vice versa. Considering *A2* and B^2, changes in *A* or *B* cause linear changes in the Module and Stress, and a non-linear change in elongation. In the case of swelling, it seems that it might be affected non-linearly by changes in *A* or *B*. Interestingly, changes in *A* showed higher non-linear changes in degradation compared to changes in *B*. As a general conclusion, it can be claimed that changes in *A* and *B* result in a non-linear reduction for all responses but Module.

Given the findings from the previously discussed aspects, the R1 formulation, distinguished by its superior mechanical properties, increased swelling, and prolonged degradation, was selected to produce the final RCNP-loaded patch. This patch will subsequently be subjected to further investigations of release efficacy under various pH conditions, biocompatibility, and infection detection analysis.

The release study was initially conducted for pure RCNPs and subsequently for RCNP-loaded patches. Figs. 6D and 7A indicate that RCNPs exhibit pH-responsive release of RB, which aligns with findings by Unsoy et al. concerning doxorubicin (DOX) release from chitosan nanoparticles [55]. This release mechanism commences with water diffusing into the NP structure, leading to swelling. RB diffusion subsequently occurs through the RCNP matrix, accompanied by polymer degradation and/or erosion, resulting in RB release [56]. Notably, the rate of RB release from RCNPs was highest in a basic environment and lowest in an acidic solution, indicating an increase in RB delivery with increasing pH. Furthermore, the results of RB release from RCNP-loaded patches (Fig. 7B) exhibited a similar trend, with RB release being lower than that of the free RCNPs. This variance is attributed to the RB diffusing from the RCNP into the SA layer and then into the environment (water) in the case of RCNP-loaded patches. In contrast, with RCNPs, the RB directly traverses the RCNP matrix into the environment. Notably, the RCNP-loaded patches also exhibited pH-responsive release behavior.

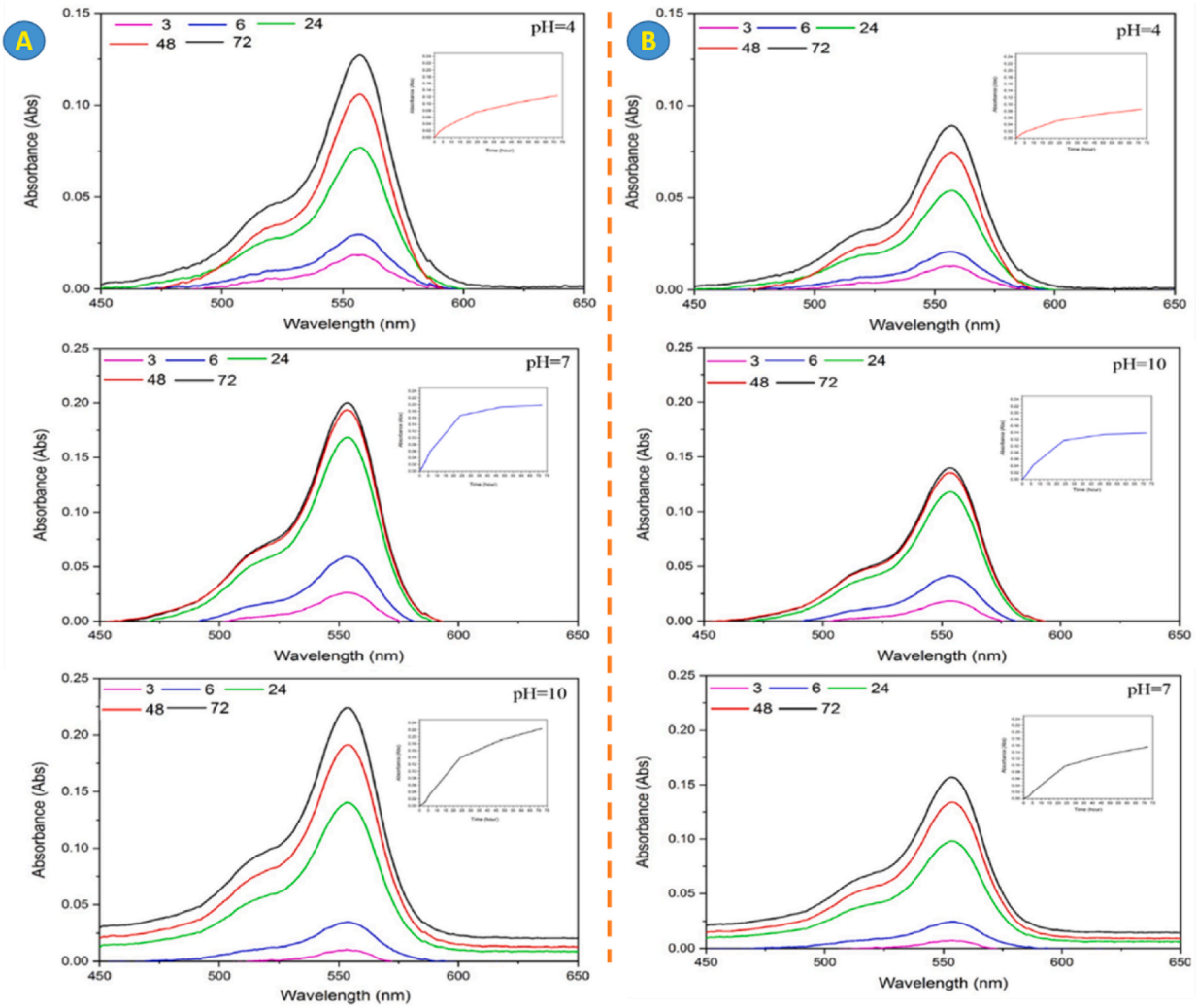

Fig. 7. RB release profile for A) RCNPs and B) RCNP-loaded films at different pH values at room temperature.

Research by Soheila and Saleh indicated that alginate gel shrinkage increases with increasing pH. Furthermore, studies have demonstrated that the viscosity of alginate solution increases under acidic conditions due to its reduced solubility in acidic environments. In such situations, carboxyl groups protonate in the matrix, forming less hydrophilic acid structures [57].

Fig. 8A shows the biocompatibility results for the RCNP-loaded patch, and the results demonstrated that the patch showed good cell viability with no cytotoxicity. This means that RCNPs do not affect cell proliferation or population and that the final patch is entirely biocompatible. Zhang et al. (2017) investigated the biocompatibility of nanoparticle-loaded patches for drug delivery. Like our findings, they reported that their patches resulted in high cell viability and no significant cytotoxicity. This suggests that when properly integrated, nanoparticles do not adversely affect cell health [58].

A novel patch design (Fig. 3A) was created based on the selected formula, featuring a restructured arrangement and embedding of RCNPs. In this design, any alterations in the geometry of the RCNP area (circular) serve as an infection indicator. To assess its efficacy, the patch's performance was tested against two bacterial strains: *Escherichia coli* (gram-positive) and *Staphylococcus aureus* (gram-negative). These bacteria were cultured at 37 °C for 48 h. As depicted in Fig. 8B, *Staphylococcus aureus* increased the environmental pH, consequently triggering the release of RB from the RCNP-loaded patch. This release disrupted the regular arrangement of the RCNPs. Fig. 8B also illustrates the same trend for *E. coli*. Maintaining pH control at the wound site is vital in healing [59]. Healthy skin typically has a slightly acidic pH, generally between 5 and 6, while wounded skin tends to have a relatively higher pH, around 7.4 [59,60]. In chronic wounds, the pH can increase further, often exceeding 7.4, due to alkaline byproducts generated by microbial activity in the wound environment [60]. This elevated pH can impede the wound healing process, as healing in an alkaline environment is generally slower and more prone to complications [61]. Conventional pH measurement techniques—such as electrodes, pH paper, or cotton swabs—have limitations, primarily because they require removal of the wound dressing and direct contact with the wound site. This contact can lead to discomfort, potential tissue damage, and an increased risk of infection, all of which may delay healing [62]. To address these challenges, there is a growing interest in developing smart wound dressings that can monitor pH changes without necessitating the removal of the dressing. Researchers have explored various pH-sensitive wound dressings that rely on visible color changes to signal pH variations, aiming for a non-invasive and user-friendly solution [62,63]. Clemens et al. provide an extensive overview of this area [64].

In dye-based wound dressings, pH-sensitive color changes are often employed as indicators. Yet, color shifts can be imprecise, particularly when slight pH alterations lead to only minimal hue changes. To enhance accuracy and functionality in detection, alternative methods have been developed. In our research, we integrated RCNP nanoparticles into the dressing, arranging them in a

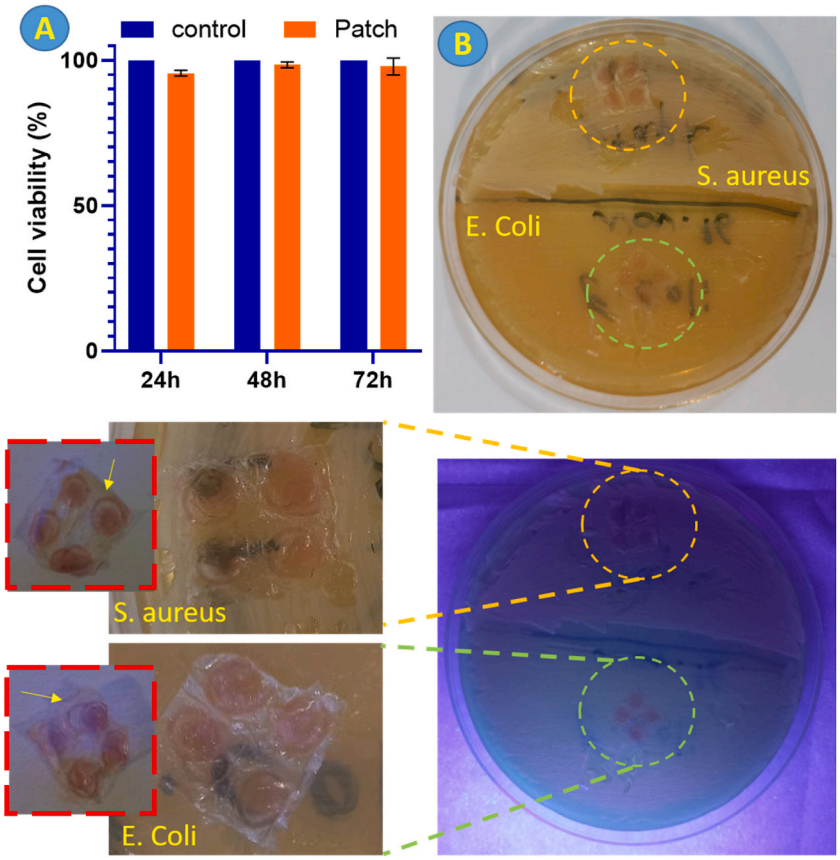

Fig. 8. A) Cell viability results after 24 h, 48 h, and 72 h. B) Visual assessment of the infection detection ability of the RCNP-loaded patch.

distinct circular pattern with precisely four nanoparticles per patch. This arrangement allows for a refined detection mechanism based on a pH-responsive reaction: as pH levels rise within the wound environment, the nanoparticles initiate a coordinated movement, triggering an intensified release of RB. This release disrupts the nanoparticles' initial configuration, resulting in a visible geometric transformation of the patch structure. Unlike subtle color changes, this geometric shift provides a reliable and discernible response, allowing for easier identification and minimizing the ambiguity associated with pH-sensitive hues. Our results demonstrate a positive correlation between elevated wound pH and the quantity of RB released, confirming that the patch effectively responds to pH increases. This innovative method not only offers greater precision in wound monitoring but also shows potential for predicting bacterial activity by responding to pH elevation, presenting a more accurate and adaptive tool for clinical applications.

4. Conclusions and prospects

This study aimed to develop an innovative color-based wound dressing capable of detecting infections through changes in geometry. The approach involved synthesizing RCNPs, measuring 300–400 nm, via ion gelation. These nanoparticles were then incorporated into a unique SA film arrangement. The wound dressing, which was composed of SA and CNPs loaded with rhodamine, effectively released the dye at a concentration of 0.000001 g/ml over 24 h. CNPs and SA significantly influenced the release behavior and properties of the wound dressing. The mechanical testing results indicated that the R1 formula exhibited favorable mechanical properties. The final patch demonstrated responsiveness to both gram-positive and gram-negative microorganisms. Consequently, when designed with the proposed strategy, this biodegradable patch holds promise for infection diagnosis.

The development of this smart wound dressing represents a significant advancement in wound care technology. By incorporating RB-loaded RCNPs into an SA patch, this study introduced a biocompatible and responsive WD capable of real-time infection detection through visible color changes. This innovative approach can significantly enhance infection management in clinical settings, improve patient outcomes and increase the effectiveness of wound healing processes. The biodegradable nature of the patch further underscores its potential for widespread clinical application, offering a sustainable solution for advanced wound care.

For future studies, the use of novel nanoparticles, such as MOFs, which are known for their high loading capacity, is recommended. Employing 3D bioprinting techniques to create alternative nanoparticle arrangements could offer more efficient and rapid detection. Finally, a valuable avenue for future research involves comparing this strategy in wound dressings made from hydrophilic, hydrophobic biomaterials, or a combination of both.

CRediT authorship contribution statement

Seyed Alireza Sheikholeslami: Writing – original draft, Software, Methodology. **Javad Esmaeili:** Writing – review & editing, Visualization, Validation, Software, Methodology. **Saeedeh Zare Jalise:** Writing – review & editing, Visualization, Validation, Software, Methodology. **Aboulfazl Barati:** Writing – review & editing, Supervision, Project administration, Methodology, Conceptualization.

Data and code availability

Data will be made available on request.

Declaration of competing interest

The authors declare that they have no known competing financial interests or personal relationships that could have appeared to influence the work reported in this paper.

Acknowledgment

This research received no specific grant from funding agencies in the public, commercial, or not-for-profit sectors. However, we highly thank TISSUEHUB Co. for scientifically supporting this project.

References

[1] A.R. Abbasi, et al., Bioinspired sodium alginate based thermosensitive hydrogel membranes for accelerated wound healing, Int. J. Biol. Macromol. 155 (2020) 751–765.
[2] I. George Broughton, J.E. Janis, C.E. Attinger, The basic science of wound healing, Plast. Reconstr. Surg. 117 (7S) (2006) 12S–34S.
[3] P. Martin, R. Nunan, Cellular and molecular mechanisms of repair in acute and chronic wound healing, Br. J. Dermatol. 173 (2) (2015) 370–378.
[4] L. Yildirimer, N.T. Thanh, A.M. Seifalian, Skin regeneration scaffolds: a multimodal bottom-up approach, Trends Biotechnol. 30 (12) (2012) 638–648.
[5] M.C. Robson, Wound infection: a failure of wound healing caused by an imbalance of bacteria, Surg. Clin. 77 (3) (1997) 637–650.
[6] G. Dow, A. Browne, R. Sibbald, Infection in chronic wounds: controversies in diagnosis and treatment, Ostomy/Wound Manag. 45 (8) (1999), 23-7, 29.
[7] V.B. Carruthers, P.A. Cotter, C.A. Kumamoto, Microbial pathogenesis: mechanisms of infectious disease, Cell Host Microbe 2 (4) (2007) 214–219.
[8] S. Li, et al., Diagnostics for wound infections, Adv. Wound Care 10 (6) (2021) 317–327.
[9] C. Xu, et al., Nanoparticle-based wound dressing: recent progress in the detection and therapy of bacterial infections, Bioconjugate Chem. 31 (7) (2020) 1708–1723.
[10] J. Zhou, et al., Development of a prototype wound dressing technology which can detect and report colonization by pathogenic bacteria, Biosens. Bioelectron. 30 (1) (2011) 67–72.

[11] N. Thet, et al., Prototype development of the intelligent hydrogel wound dressing and its efficacy in the detection of model pathogenic wound biofilms, ACS Appl. Mater. Interfaces 8 (24) (2016) 14909–14919.
[12] B. Qiao, et al., Smart wound dressing for infection monitoring and NIR-triggered antibacterial treatment, Biomater. Sci. 8 (6) (2020) 1649–1657.
[13] M. Agarwal, et al., Preparation of chitosan nanoparticles and their in-vitro characterization, Int. J. Life Sci. Sci. Res. 4 (2) (2018) 1713–1720.
[14] Y. Gong, et al., Preparation of alginate membrane for tissue engineering, J. Polym. Eng. 36 (4) (2016) 363–370.
[15] C. Badita, et al., Characterization of sodium alginate based films, Rom. J. Phys. 65 (2020) 1–8.
[16] A.S. Giz, et al., Stress relaxation and humidity dependence in sodium alginate-glycerol films, J. Mech. Behav. Biomed. Mater. 100 (2019) 103374.
[17] R. Russo, M. Malinconico, G. Santagata, Effect of cross-linking with calcium ions on the physical properties of alginate films, Biomacromolecules 8 (10) (2007) 3193–3197.
[18] A.A. Arafa, et al., Preparation and characterization of smart therapeutic pH-sensitive wound dressing from red cabbage extract and chitosan hydrogel, Int. J. Biol. Macromol. 182 (2021) 1820–1831.
[19] J. Yang, et al., Intelligent wound dressing for simultaneous in situ detection and elimination of pathogenic bacteria, Acta Biomater. 174 (2024) 177–190.
[20] G.S. El-Feky, et al., Using chitosan nanoparticles as drug carriers for the development of asilver sulfadiazine wound dressing, Carbohydr. Polym. 158 (2017) 11–19.
[21] P.O. Stănescu, et al., Novel chitosan and bacterial cellulose biocomposites tailored with polymeric nanoparticles for modern wound dressing development, Drug Deliv. 28 (1) (2021) 1932–1950.
[22] S. Pradhan, S. Mohanty, S.K. Nayak, In-situ aerobic biodegradation study of epoxy-acrylate film in compost soil environment, J. Polym. Environ. 26 (2018) 1133–1144.
[23] H. Suryanto, A.S. Pahlevi, U. Yanuhar, Effect of bacterial cellulose reinforcement on morphology and tensile properties of starch-based biocomposite, in: IOP Conference Series: Materials Science and Engineering, IOP Publishing, 2021.
[24] M.A. Siddiqui, et al., Molybdenum nanoparticles-induced cytotoxicity, oxidative stress, G2/M arrest, and DNA damage in mouse skin fibroblast cells (L929), Colloids Surf. B Biointerfaces 125 (2015) 73–81.
[25] Z. Song, et al., Dual-mode detection of cysteamine using Ag nanoparticle-riboflavin composites, ACS Appl. Nano Mater. 7 (7) (2024) 6995–7007.
[26] B.-c. Wu, D.J. McClements, Design of reduced-fat food emulsions: manipulating microstructure and rheology through controlled aggregation of colloidal particles and biopolymers, Food Res. Int. 76 (2015) 777–786.
[27] A. Shahzad, et al., Formulation development and characterization of cefazolin nanoparticles-loaded cross-linked films of sodium alginate and pectin as wound dressings, Int. J. Biol. Macromol. 124 (2019) 255–269.
[28] Y.B. Bhagath, et al., Effect of sulfamerazine on structural characteristics of sodium alginate biopolymeric films, Biotechnol. Bioproc. Eng. 27 (4) (2022) 596–606.
[29] K. Li, et al., Preparation of chitosan-sodium alginate films through layer-by-layer assembly and ferulic acid crosslinking: film properties, characterization, and formation mechanism, Int. J. Biol. Macromol. 122 (2019) 485–492.
[30] R. Kumar, et al., Surface coating and functionalization of metal and metal oxide nanoparticles for biomedical applications, in: Metal Oxides for Biomedical and Biosensor Applications, Elsevier, 2022, pp. 205–231.
[31] L.-Y. Chen, et al., Processing and properties of magnesium containing a dense uniform dispersion of nanoparticles, Nature 528 (7583) (2015) 539–543.
[32] S.A. Kahdestani, M.H. Shahriari, M. Abdouss, Synthesis and characterization of chitosan nanoparticles containing teicoplanin using sol–gel, Polym. Bull. 78 (2) (2021) 1133–1148.
[33] K. Divya, et al., Antimicrobial properties of chitosan nanoparticles: mode of action and factors affecting activity, Fibers Polym. 18 (2) (2017) 221–230.
[34] I. Leceta, et al., Characterization and antimicrobial analysis of chitosan-based films, J. Food Eng. 116 (4) (2013) 889–899.
[35] R.A. Mauricio-Sánchez, et al., FTIR spectroscopy studies on the spontaneous neutralization of chitosan acetate films by moisture conditioning, Vib. Spectrosc. 94 (2018) 1–6.
[36] Y. Osuna, et al., Chitosan-coated magnetic nanoparticles with low chitosan content prepared in one-step, J. Nanomater. (2012) 2012.
[37] A.A. Inyinbor, F.A. Adekola, G.A. Olatunji, Adsorption of Rhodamine B dye from aqueous solution on Irvingia gabonensis biomass: kinetics and thermodynamics studies, S. Afr. J. Chem. 68 (2015) 115–125.
[38] Y. Zhang, et al., New near-infrared rhodamine dyes with large Stokes shifts for sensitive sensing of intracellular pH changes and fluctuations, Chem. Commun. 54 (55) (2018) 7625–7628.
[39] S. Kalia, et al., Exploring fungal-mediated solutions and its molecular mechanistic insights for textile dye decolorization, Chemosphere 360 (2024) 142370.
[40] Y. Lu, et al., Adsorption of rhodamine B from aqueous solution by goat manure biochar: kinetics, isotherms, and thermodynamic studies, Pol. J. Environ. Stud. 29 (4) (2020).
[41] L.T.K. Ngan, et al., Preparation of chitosan nanoparticles by spray drying, and their antibacterial activity, Res. Chem. Intermed. 40 (6) (2014) 2165–2175.
[42] J. Liu, et al., Sensitive detection of Au(III) using regenerative rhodamine B–functionalized chitosan nanoparticles, Sensor. Actuator. B Chem. 233 (2016) 361–368.
[43] E. Gryparis, et al., Effect of conditions of preparation on the size and encapsulation properties of PLGA-mPEG nanoparticles of cisplatin, Drug Deliv. 14 (6) (2007) 371–380.
[44] A. Sweity, et al., pH effects on the adherence and fouling propensity of extracellular polymeric substances in a membrane bioreactor, J. Membr. Sci. 378 (1–2) (2011) 186–193.
[45] M. Shirangi, B. Michel, Mechanism of moisture diffusion, hygroscopic swelling, and adhesion degradation in epoxy molding compounds, in: Moisture Sensitivity of Plastic Packages of IC Devices, Springer, 2010, pp. 29–69.
[46] M. Mahmud, et al., Degradation of chitosan by gamma ray with presence of hydrogen peroxide, in: AIP Conference Proceedings., American Institute of Physics, 2014.
[47] L. Zhang, S.J. Rowan, Effect of sterics and degree of cross-linking on the mechanical properties of dynamic poly (alkylurea–urethane) networks, Macromolecules 50 (13) (2017) 5051–5060.
[48] A. Jafari, et al., Effect of organic/inorganic nanoparticles on performance of polyurethane nanocomposites for potential wound dressing applications, J. Mech. Behav. Biomed. Mater. 88 (2018) 395–405.
[49] R. Peng, et al., Modeling of nano-reinforced polymer composites: microstructure effect on Young's modulus, Comput. Mater. Sci. 60 (2012) 19–31.
[50] Y. Zare, Assumption of interphase properties in classical Christensen–Lo model for Young's modulus of polymer nanocomposites reinforced with spherical nanoparticles, RSC Adv. 5 (116) (2015) 95532–95538.
[51] L. Wang, et al., Mussel-inspired conductive cryogel as cardiac tissue patch to repair myocardial infarction by migration of conductive nanoparticles, Adv. Funct. Mater. 26 (24) (2016) 4293–4305.
[52] A. Jonderian, R. Maalouf, Formulation and in vitro interaction of rhodamine-B loaded PLGA nanoparticles with cardiac myocytes, Front. Pharmacol. 7 (2016) 458.
[53] L.-P. Wang, et al., Rhodamine B-loaded star polystyrenes and their luminescent honeycomb-patterned porous films, React. Funct. Polym. 99 (2016) 59–64.
[54] S. Jadbabaei, et al., Preparation and characterization of sodium alginate-PVA polymeric scaffolds by electrospinning method for skin tissue engineering applications, RSC Adv. 11 (49) (2021) 30674–30688.
[55] G. Unsoy, et al., Synthesis of Doxorubicin loaded magnetic chitosan nanoparticles for pH responsive targeted drug delivery, Eur. J. Pharmaceut. Sci. 62 (2014) 243–250.
[56] M.A. Mohammed, et al., An overview of chitosan nanoparticles and its application in non-parenteral drug delivery, Pharmaceutics 9 (4) (2017).
[57] H.-Y. Park, et al., Effect of pH on drug release from polysaccharide tablets, Drug Deliv. 5 (1) (1998) 13–18.
[58] Z. Zhang, et al., Biocompatible 5-Aminolevulinic Acid/Au nanoparticle-loaded ethosomal vesicles for in vitro transdermal synergistic photodynamic/photothermal therapy of hypertrophic scars, Nanoscale Res. Lett. 12 (2017) 1–11.

[59] N. Pan, et al., Color-changing smart fibrous materials for naked eye real-time monitoring of wound pH, J. Mater. Chem. B 7 (16) (2019) 2626–2633.
[60] L.A. Schneider, et al., Influence of pH on wound-healing: a new perspective for wound-therapy? Arch. Dermatol. Res. 298 (9) (2007) 413–420.
[61] S.L. Percival, et al., The effects of pH on wound healing, biofilms, and antimicrobial efficacy, Wound Repair Regen. 22 (2) (2014) 174–186.
[62] S. Ono, et al., Increased wound pH as an indicator of local wound infection in second degree burns, Burns 41 (4) (2015) 820–824.
[63] C. Schaude, et al., The development of indicator cotton swabs for the detection of pH in wounds, Sensors 17 (6) (2017) 1365.
[64] C. Gamerith, et al., pH-responsive materials for optical monitoring of wound status, Sensor. Actuator. B Chem. 301 (2019) 126966.